



ENERGY MATERIALS Cite This: ACS Appl. Energy Mater. 2020, 3, 411–422

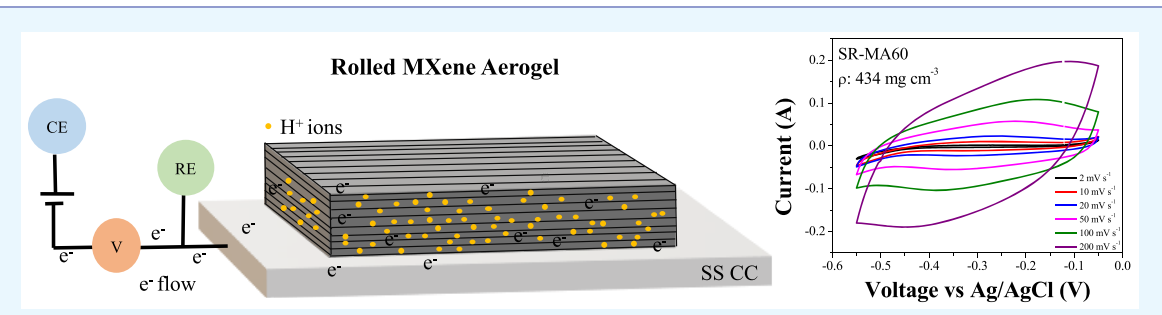
www.acsaem.org

Article

MXene Tunable Lamellae Architectures for Supercapacitor **Electrodes**

Vildan Bayram,[†] Michael Ghidiu,[§] Jae J. Byun,[†] Shelley D. Rawson,[‡] Pei Yang,[†] Samuel A. Mcdonald,^{‡,||} Matthew Lindley,[†] Simon Fairclough,[†] Sarah J. Haigh,[†] Philip J. Withers,[†],[‡] Michel W. Barsoum,[§] Ian A. Kinloch, and Suelen Barg*, b

Supporting Information



ABSTRACT: The rich elemental composition, surface chemistry, and outstanding electrical conductivity of MXenes make them a promising class of two-dimensional (2D) materials for electrochemical energy storage. To translate these properties into high performance devices, it is essential to develop fabrication strategies that allow MXenes to be assembled into electrodes with tunable architectures and investigate the effect of their pore structure on the capacitive performance. Here, we report on the fabrication of MXene aerogels with highly ordered lamellar structures by unidirectional freeze-casting of additive-free Ti₃C₂T_x. aqueous suspensions. These structures can be subsequently processed into practical supercapacitor electrode films by pressing or calendering steps. This versatile processing route allows a wide control of film thickness, spacing within lamellae (to give electrolyte accessible sites), and densities (over 2 orders of magnitude) and hence gives control over the final properties. The asprepared MXene aerogel with a density of 13 mg cm⁻³ achieves 380 F g⁻¹ capacitance at 2 mV s⁻¹ and 75 F g⁻¹ at 50 mV s⁻¹. The calendering of the MXene aerogel into a porous 60 μ m thick film with a density of 434 mg cm⁻³ leads to a superior rate capability of 309 F g⁻¹ at 50 mV s⁻¹. In addition, the rolled electrodes present an improvement in volumetric capacitance of 104 times as compared to the as-prepared MXene aerogel. Finally, the outstanding cyclability of rolled electrodes strengthens their nomination for supercapacitor applications. In this paper we demonstrate the possibilities in tuning the porosity and the electrochemical properties of aerogels highlighting the importance of evaluating new and hybrid processing methods to develop energy storage applications. The simplicity and versatility of the developed fabrication strategy open opportunities for the utilization of MXene lamellae architectures in a wide range of applications requiring controlled porosity including catalysis, filtration, and water purification.

KEYWORDS: MXene, freeze-casting, supercapacitor electrodes, aerogels, energy storage

INTRODUCTION

The increasing demand for energy storage devices with high energy densities and power capabilities has triggered research into more efficient and durable electrode materials. 1-6 Studies have demonstrated that the utilization of MXenes as supercapacitor electrode materials can provide outstanding capacitances and quite good cycle lives. 7,8 This capacitive performance is attributed to their unique structural configuration which combines conductive transition metal carbide layers that enable fast electron transfer with an oxygenated

surface that both provides redox-active sites9 and allows the intercalation of water for improved ion transport. 10,11 MXenes are synthesized by the extraction of the "A" layers from the layered carbides, nitrides, or carbonitrides which are known as MAX phases. 12-15 These phases have the general formula $M_{n+1}AX_n$ (n = 1, 2, 3), where M represents a transition metal,

Received: August 26, 2019 Accepted: December 2, 2019 Published: December 2, 2019



411

[†]Department of Materials and [‡]The Henry Royce Institute, Department of Materials, University of Manchester, Manchester M13 9PL, U.K.

[§]Department of Materials Science and Engineering and A. J. Drexel Nanomaterials Institute, Drexel University, Philadelphia, Pennsylvania 19104, United States

European Synchrotron Radiation Facility (ESRF), 71 Avenue des Martyrs, 38000 Grenoble, France

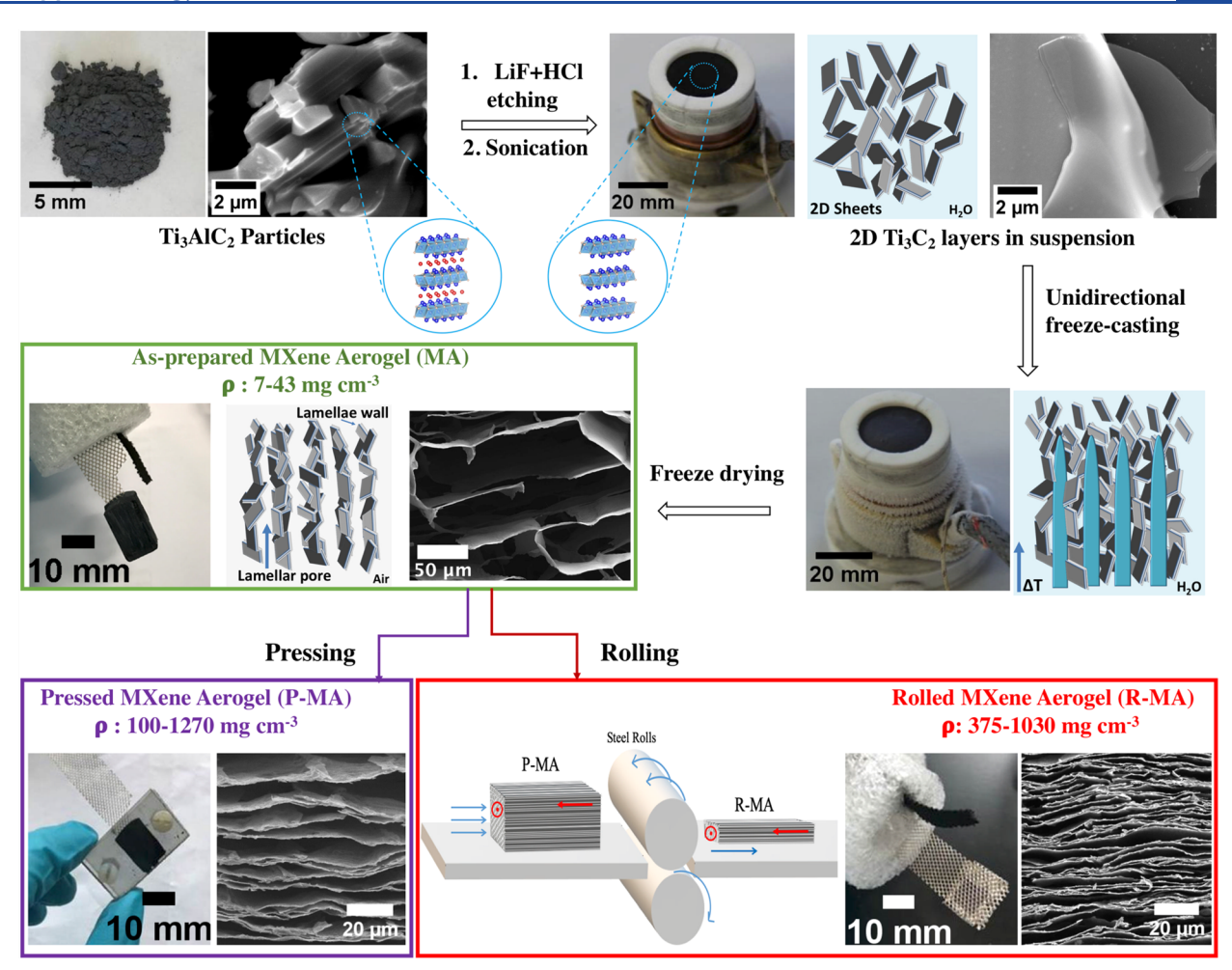


Figure 1. Schematics and images of the fabrication strategy to produce $Ti_3C_2T_x$ aerogels and supercapacitor electrodes by using three different approaches. From top left of the image following the arrows: optical photographs and SEM images of Ti_3AlC_2 particles; image of the mold on top of the freeze caster (detailed image in Figure S1) containing the 2D $Ti_3C_2T_x$ suspension (aqueous suspensions is schematically illustrated) and corresponding SEM image of a few layers sheet; unidirectional freeze-cast sample inside the mold (schematic of the microstructure formation during ice crystal growth); optical photographs and SEM images of electrode layers in the form of as-prepared MA (lamellae architecture formed within the aerogel is schematically illustrated), pressed (P-MA) and rolled $Ti_3C_2T_x$ aerogel (R-MA). The range of electrode densities (ρ) achieved by each approach is also indicated. More details on the evolution of MA into P-MA and R-MA are shown in Figure S2. The red vectors inserted in the SEM images indicate the freezing direction.

A represents a IIIA or IVA group element, and X stands for C and/or N. The process of selectively etching the A layer creates 2D MXene layers terminated with oxygen and/or fluorine functional groups.

Conventionally, MXene electrodes are fabricated via vacuum filtration which induces "planar" restacking of MXene flakes. 17,18 The resulting MXene film electrodes possess high densities that results in exceptional volumetric capacitance values while achieving comparatively lower gravimetric capacitance values (900 F cm⁻³ and 245 F g⁻¹ at 2 mV s⁻¹ in H₂SO₄¹⁰) and low rate capability as a result of poor ion transport within the stacked electrode structure. Designing hierarchically structured electrodes could potentially overcome these limitations. 19-21 The strategies that have been proposed to create such MXene-based structures can be grouped as (1) introducing other 2D materials as spacers between MXene flakes to avoid their restacking, 19,22,23 (2) separating MXene layers with surfactants, (3) creating porous structures via additional chemical and thermal processes in parallel with vacuum filtration, 11,25,26 (4) creating 3D crumpled MXene structures via spray drying and other approaches, 27,28 and (5)

building aerogels with chemically and thermally assisted templating approaches. ^{21,29} Although these methods offer the potential to modify microstructural design to improve the performance of MXene electrodes, there are still several drawbacks that limit their wider application. For example, most of the aforementioned methods are not versatile in terms of porosity control, involve different additives, chemical and/or thermal processes, lead to a change of the surface composition, and/or deteriorate the electrical conductivity of the materials. As an alternative, the use of freeze-drying methods to build porous MXene structures has been mentioned recently in the literature. 29-32 One of these methods used a bidirectional freeze-casting to produce lamellae anisotropic aerogels for a different application.³² Although they used the mold geometry to control it which limits the shape and microstructure of the materials produced, there was no control in freezing rate as done here. Unidirectional freeze-casting to build MXene architectures and study the effect of the freeze casting parameters to tune the microstructure and electrochemical properties of MXene electrodes has not yet been reported. Freeze-casting is a versatile method that is capable of

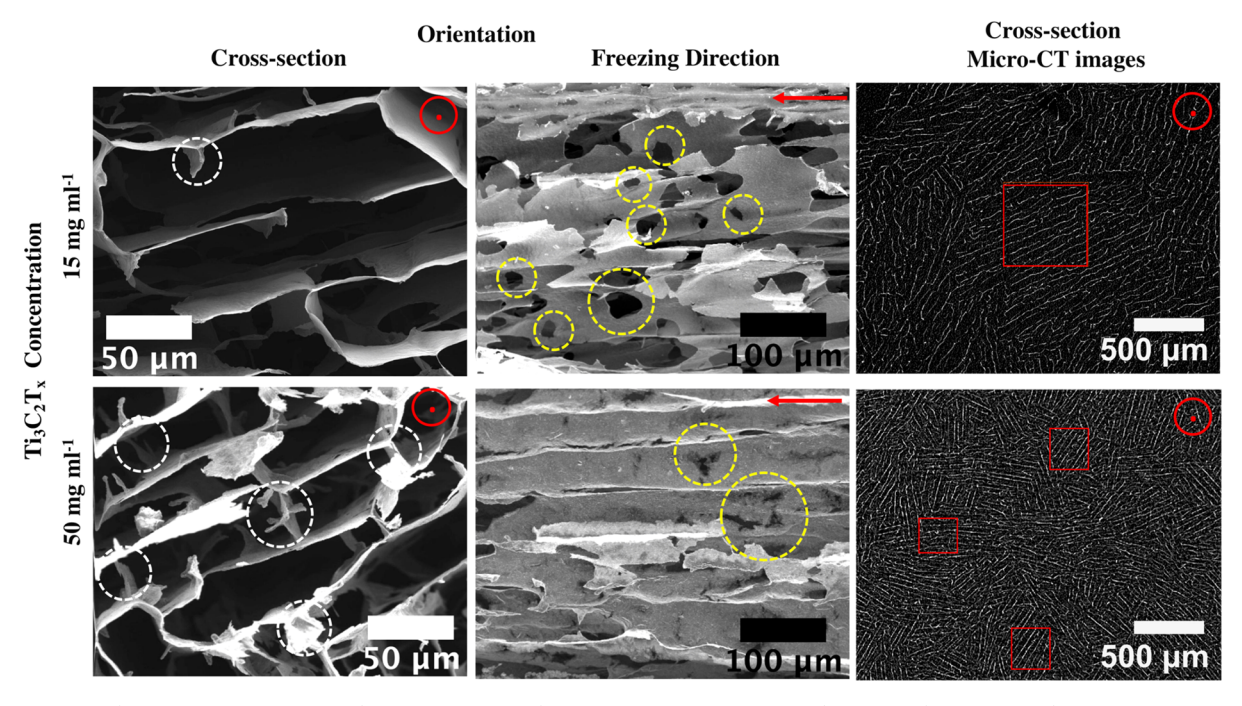


Figure 2. SEM (left and middle columns) and Micro-CT (micro computed tomography) images (right column) of MAs prepared from suspensions with varying $Ti_3C_2T_x$ concentrations (labeled on the left side of the images as 15 and 50 mg mL⁻¹). Images were taken at different orientations (viewing direction is labeled on top of the image, and the freezing direction is indicated by the red inserted vectors). The bridges connecting the lamellae are identified with white circles in the cross-sectional images. The openings within the lamellae are identified with yellow circles in the freezing direction images. Some of the lamellae domains are indicated in the Micro-CT images with red squares. Each domain presents a distinct orientation of the lamellae structure. Suspensions were frozen at 2.5 °C min⁻¹ (more details in Table S1).

modifying the size and shape of pores in the material, which directly allows the manipulation of mechanical and electrical properties of the resulting porous structures.^{33–39} Freezecasting of MXene electrodes can provide a practical route to tune their internal microstructure and broaden our understanding of the relationship between the electrode architecture and its capacitive performance.

In this work, MXene aerogels with lamellar architectures are produced by the unidirectional freeze-casting of additive-free 2D ${\rm Ti_3C_2T_x}$ aqueous colloidal suspensions. We discuss the effect of processing conditions on aerogel architectures and how this can be used to tune their gravimetric capacitance. Subsequent pressing and calendaring are used to optimize the volumetric capacitance and rate capabilities of the electrodes. This versatile fabrication approach can guide the development of practical MXene supercapacitors and other applications of porous functional materials beyond energy.

■ RESULTS AND DISCUSSION

Fabrication of MXene Tunable Lamellae Architectures. The fabrication strategy (Figure 1) is based on the preparation of additive-free 2D ${\rm Ti_3C_2T_x}$ aqueous colloidal suspensions at pH 5–6 (zeta potential between -23 and -28 mV)⁴⁰ that are subsequently frozen unidirectionally using a lab-built freeze caster (details in the Methods section and Figure S1) to allow the formation of robust and lightweight asprepared MXene aerogels (MA). MAs with the highest electrochemical performance are selected and subsequently compressed (P-MA) or rolled (R-MA) via calendering (Figure S2) to form practical electrode films with reduced spacing between the lamellae architectures (Figure 1, Figures S2 and S3).

Few layers thick (~4 nm) 2D Ti₃C₂T_xflakes, with lateral sizes ranging from 0.5 to 5 μ m (Figure S4), is incorporated into suspension formulations with concentrations ranging from 5 to 50 mg mL⁻¹ and are processed using freezing conditions of 2.5 or 5 °C min⁻¹ (Table S1), which allowed lamellar ice crystal growth. During directional freezing of these suspensions, the growing ice crystals control the arrangement of the 2D flakes in the water (within neighboring crystals). The ice shape and size templates the spacing (pores) within the $Ti_3C_2T_x$ consolidated walls of MAs after freeze-drying (Figures 1 and 2, Figure S5). The walls are formed by 1-18 atomic layers of Ti₃C₂T_x, as determined by cross-sectional annular dark-field (ADF) STEM images (Figure 2, Figures S6 and S7). The less ordered nature of 2D $\mathrm{Ti_3C_2T_x}^{11,41,42}$ and the stacking of fewer layers⁴³ within 3D MAs compared to films are suggested by the broadening of (002) peaks within the XRD spectrum (Figure S8). The MAs also show larger (002) dspacing values than drop-cast films as measured by XRD and by STEM (12.9 and \sim 12.5 Å, respectively).

Directional freezing allowed the fabrication of lamellar MAs with densities ranging from 7 to 43 mg cm⁻³ and porosities above 99% (Figures 2 and 3a, Table S1). The concentration of colloids in suspension directly influences the growth of ice crystals and consequently the resulting architectures. ^{33,44,45} The average lamellae spacing in the MA decreased from 53 to 32 μ m when produced from suspensions at 15–50 mg mL⁻¹ concentration (Table S1). The latter possessed a denser structure (43 mg cm⁻³) and fewer openings throughout the aerogel walls compared to the MAs fabricated from less concentrated suspensions (Figure 2). Furthermore, cross-sectional SEM images reveal that the aerogels produced from more concentrated suspensions present a higher number of bridges connecting adjacent lamellae walls. Work on

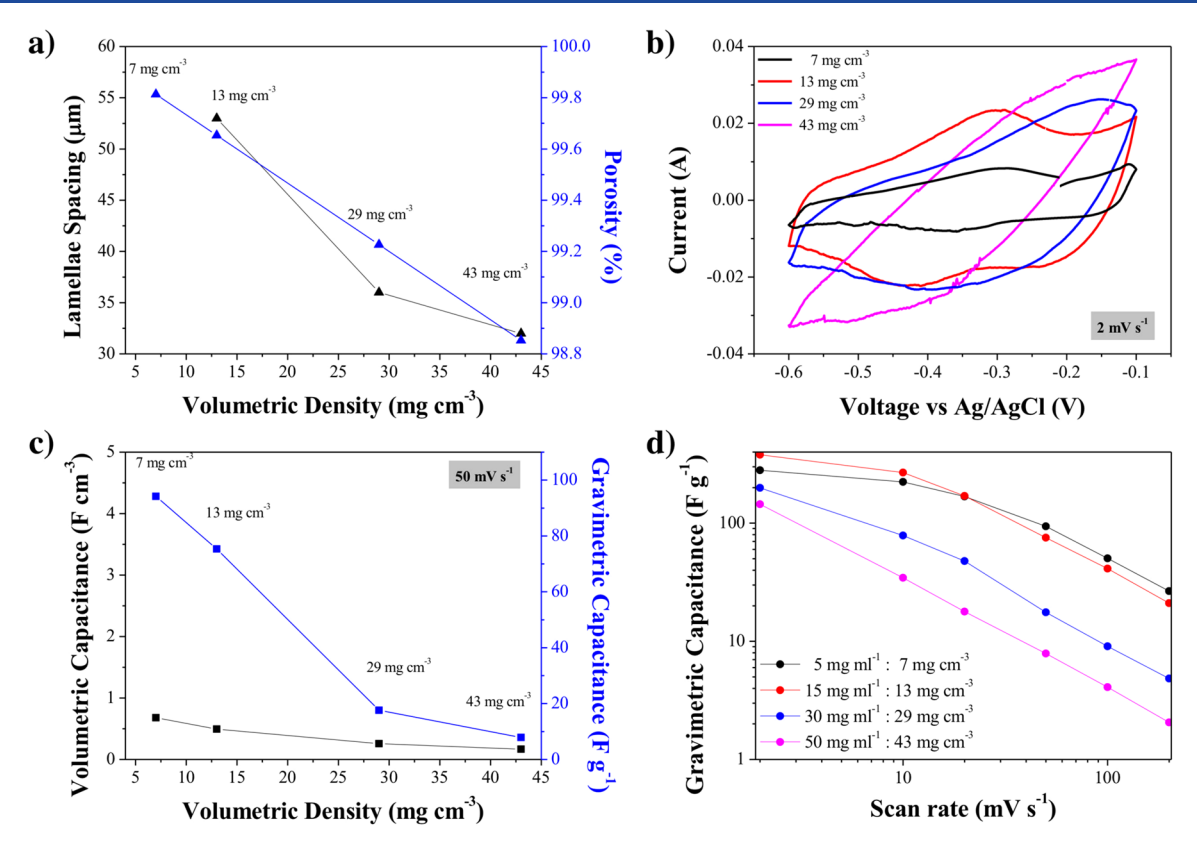


Figure 3. Electrochemical performance of as-prepared $T_{i_3}C_2T_x$ aerogels (MA) and change in porosity parameters with density. (a) Lamellae spacing measured with ImageJ from SEM images and porosity of MAs with respect to their volumetric density. (b) CV of MAs with different densities (7 up to 43 mg cm⁻³) produced from different initial suspension concentrations (5 up to 50 mg mL⁻¹ as indicated in the legend) at 2 mV s⁻¹. (c) Volumetric and gravimetric capacitance of MAs with respect to their volumetric densities at 50 mV s⁻¹. (d) Comparison of gravimetric capacitance as a function of MAs density for different scan rates (from 2 to 200 mV s⁻¹). More details on samples and their formulations are listed in Table S1.

graphene⁴⁶ and ceramic porous structures^{47–49} has also shown that colloids in highly concentrated suspensions tend to get trapped within growing crystals during ice growth which can lead to a higher density of bridges between lamellae. Micro-CT (micro computed tomography) cross-sectional images indicate that lamellae domains are larger for aerogels produced from lower concentrated suspensions (Figure 2).

Supercapacitor Application of MXene Lamellae Electrodes. Initially the effect of the internal architectures of the MAs on their electrochemical performance was studied. The porous architecture of the best performing MA type was then selected for further microstructural optimization by pressing or calendering into electrode films (Figure 1 and Figure S2 and S3).

Understanding the Effect of MA Architectural Features on Their Electrochemical Performance. The energy storage capability of MA electrode with densities from 7 to 43 mg cm⁻³ was studied in a three-electrode setup (details in the Methods section, Figure 1 and Figure S9). The structural integrity of MA electrodes was observed to be maintained through the electrochemical tests and claimed to be mechanically stable. The relationship between the MAs' volumetric density, porosity, and lamellae spacing is shown in Figure 3a. Cyclic voltammetry of the MA samples contained broad redox/intercalation peaks in the low-density MA samples (7 and 13 mg cm⁻³) at low scan rates (2 and 10 mV s⁻¹) (Figure 3b and Figure S10a,b). These peaks were found to be stable upon cycling at low scan rates (Figure

S11a); however, they vanished at higher rates, suggesting that the materials were affected by the kinetic processes as an indication of their pseudocapacitive nature. 50 The mechanism of capacitance in the MAs was evaluated by Trasatti measurements and the non-diffusion-limited contributions from the outer surface of the electrodes (EDLC and surface redox reactions, 60%) were found slightly dominant over the diffusion-limited contributions from the inner active sites (ion intercalation, 40%) (Figure S12).51 Consequently, the presence of diffusion-limited processes (H+ ion intercalation in between 2D Ti₃C₂T_r layers) was found responsible for the deviation from rectangular shape of CVs and loss in capacitance at high scan rates (Figure 3d and Figure S10).⁵¹ Furthermore, as the density of MAs increases further, even broader and less pronounced redox/intercalation peaks are visible at 2 mV s⁻¹ (Figure 3b), suggesting that MAs with higher densities also tend to become less capacitive, resulting in a lower gravimetric capacitance and lower rate capabilities (Figure 3c,d and Table S3). For example, at a scan rate of 10 mV s⁻¹, the gravimetric capacitance of the MAs drops by a factor of 6 when their density increases from 7 to 43 mg cm⁻³. In addition, the numerous bridges connecting high density MAs lamellae together with the lack of openings through the lamellae walls (Figure 2) can create a retarding effect for ion transport and contribute to the observed decrease in capacitive performance. Impedance data further show a more resistive nature for the MAs with higher density (Figure S11b).

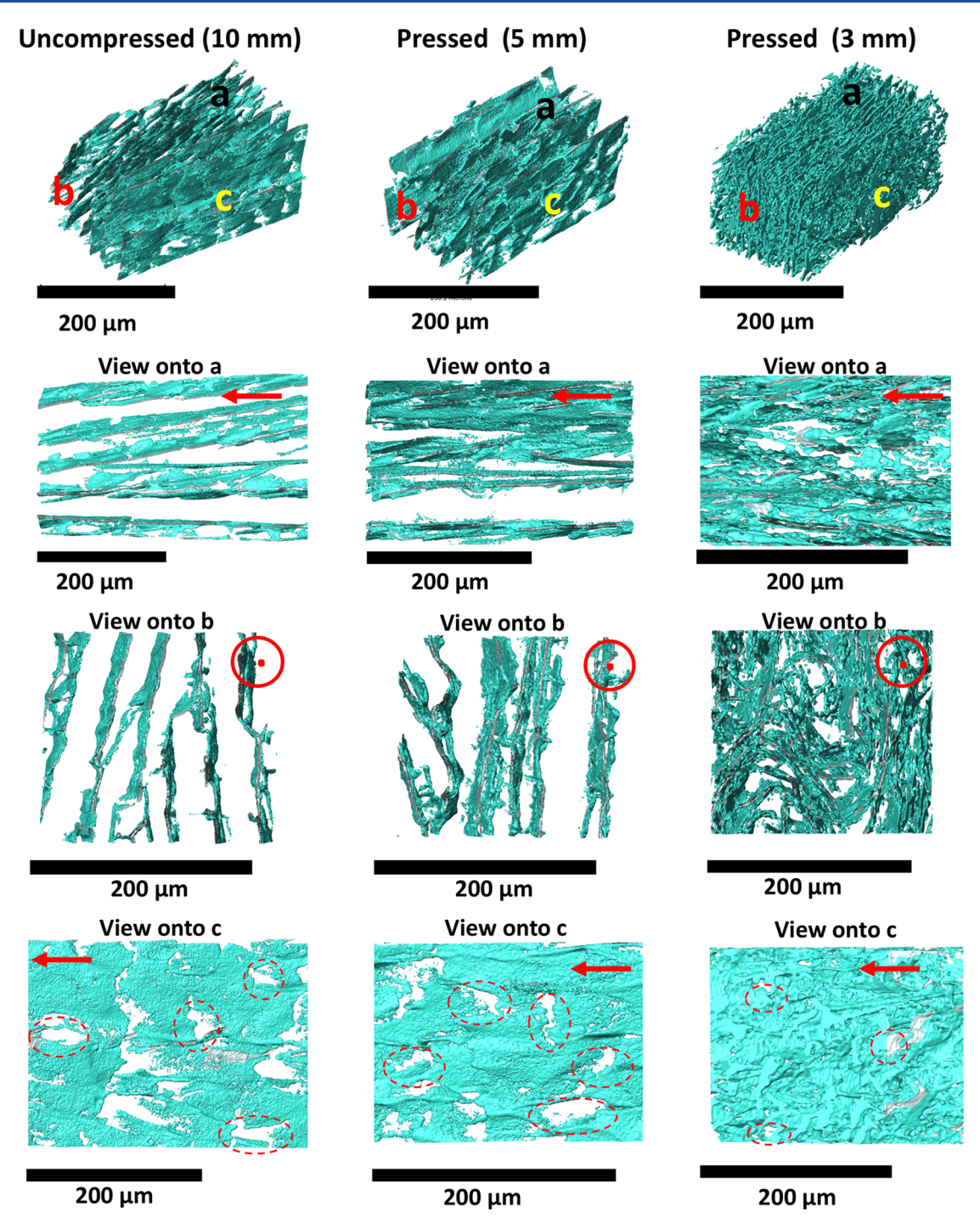


Figure 4. X-ray Micro-CT of MA and P-MA. A volume of sample was scanned with Micro-CT at three different stages: uncompressed (MA with initial thickness 10 mm), compressed down to 5 mm, and compressed down to 3 mm, from top to bottom, respectively. From top to bottom for each stage: 3D view of a region of interest; view onto a (corresponding approximately to the freezing direction) shows alignment of the sheets within the region; view onto b (corresponding to the cross section) shows the lamellae architecture; view onto c (corresponding approximately to the compression direction) shows openings within the lamellae sheets (some of these pores are indicated by red circles). Inserted red vectors indicate the freezing direction.

These results point toward the maximization of gravimetric capacitive behavior at lower density MAs as a result of key architectural features such as open, porous (numerous openings through walls) and highly continuous networks (without excessive bridging). MA with densities of 13 mg cm $^{-3}$ reached gravimetric capacitance values of 380 F g $^{-1}$ at 2 mV s $^{-1}$. The optimized internal architectures of the electrodes surpassed the capacitance of the 24 mg cm $^{-3}$ reported for a

macroporous ${\rm Ti_3C_2T_x}$ electrode produced with a sacrificial template method (330 F g⁻¹ at the same scan rate of 2 mV s⁻¹¹¹ despite our MAs being around 50 times thicker.

Optimizing the Porous Structure of MAs: Pressing and Rolling. Because of the highly porous nature of aerogels, $^{52-54}$ the freeze-cast MAs display the expected poor volumetric capacitances (Table S2, Figure 3c, and Figure S13). They further possess very large pore sizes in the range of $30-53 \mu m$

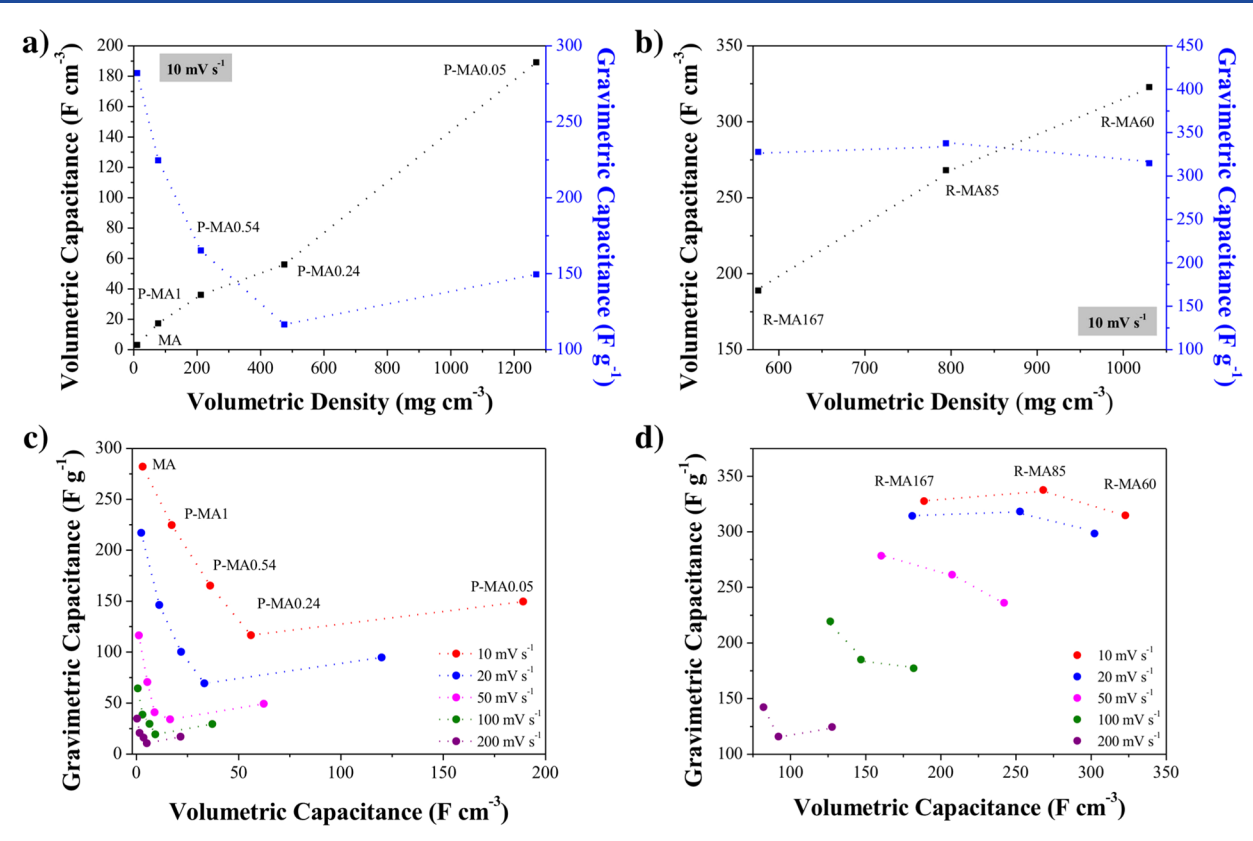


Figure 5. Electrochemical performance of pressed (P-MAs) and rolled aerogels (R-MAs). Volumetric and gravimetric capacitance of P-MAs (a) and R-MAs (b) with respect to their volumetric densities at 10 mV s⁻¹. Gravimetric capacitance as a function of volumetric capacitance at increasing scan rates (from 10 up to 200 mV s⁻¹) for P-MAs (c) and R-MAs (d). The number at the end of the sample label corresponds to their thickness after pressing (P-MAs in mm) or after calendering (R-MAs in μ m).

(Figure 3a and Table S1), and their capacitance drops significantly at higher scan rates, demonstrating the resistive nature of MAs in the electrochemical tests (Table S3). To change their pore structure and increase their volumetric capacitance and rate performances, MAs of optimized architectures (10-14 mg cm⁻³) were pressed to different thicknesses (P-MA) (Figure S2). Monitoring the microstructure along pressing with Micro-CT revealed the direct correlation between pressing and the increase in volumetric density by reduction in pore size (spacing within lamellae) (Figure 4, Figures S13, S14, and S15, and Table S2). Although pressing reduces the overall lamellae spacing within the architectures, the orientation of the lamellae within a specific domain with respect to the pressing direction seems to influence their mode of compression. For example, when MAs are compressed to 5 mm thickness, differently oriented lamellae domains are compressed to different degrees, indicating a widespread in spacing (Figure S14). Further compression of the MA to 3 mm shows a more significant change to the microstructure, with a clear reduction in pore size. View b in Figure S15 further shows regions where the lamellae loses is normal integrity due to compression.

By increasing the density of the P-MAs upon pressing (Figure S13), the volumetric capacitance gradually increases while the gravimetric capacitance drops (Figure 5a,c). The gravimetric and volumetric performance of the P-MAs deteriorate at higher rates where rapid charge/discharge characteristics are associated with electric double-layer capacitance (EDLC) and surface redox reactions (Figure 5c, Figure S16a,b, and Figure S17a-c). Trasatti measurements

of P-MAs show that the contribution from surface dominant capacitive behavior drops when compared to the other types of electrodes (MA and R-MAs) (Figure S12).55 This leads to a lower overall capacitance and an increase in the relative contributions of diffusion-controlled reactions for this type of electrode. The compression of MAs into P-MAs can lead to the disruption of the accessible areas in the electrodes (Figure 4, right column) and so contribute to these changes in the capacitive behavior. Our electrochemical characterizations show that by compressing the MAs by a factor of around 42 (from 10 to 0.24 mm thin), the gravimetric performance drops by a factor of 2 (from 282 to 116.5 F g^{-1} at 10 mV s^{-1}) and the volumetric capacitance increases by a factor of 18 (from 3.1 to 56 F cm⁻³ at 10 mV s⁻¹) (Figure 5a and Table S2). Theoretically, assuming homogeneous pressing throughout the sample and no damage to the sample with pressing, one would expect the gravimetric capacitance to be independent of pressing and the volumetric capacitance to scale linearly with the change in thickness. Micro-CT images taken at various stages upon pressing reveals during the microstructure evolution lamellae walls can crumble, leading to a substantial change of the microstructure with potential closure and/or blocking of openings within the walls as the walls get closer (Figure 4 and Figure S15). We also observed that by pressing the MA into 50 μ m thick films, the drop in gravimetric capacitance with thickness was significantly reduced. The gravimetric and volumetric capacitances of P-MA0.05 electrodes at 10 mV s⁻¹ are 149.5 F g⁻¹ and 62.3 F cm⁻³, respectively (Figure 5a,c).

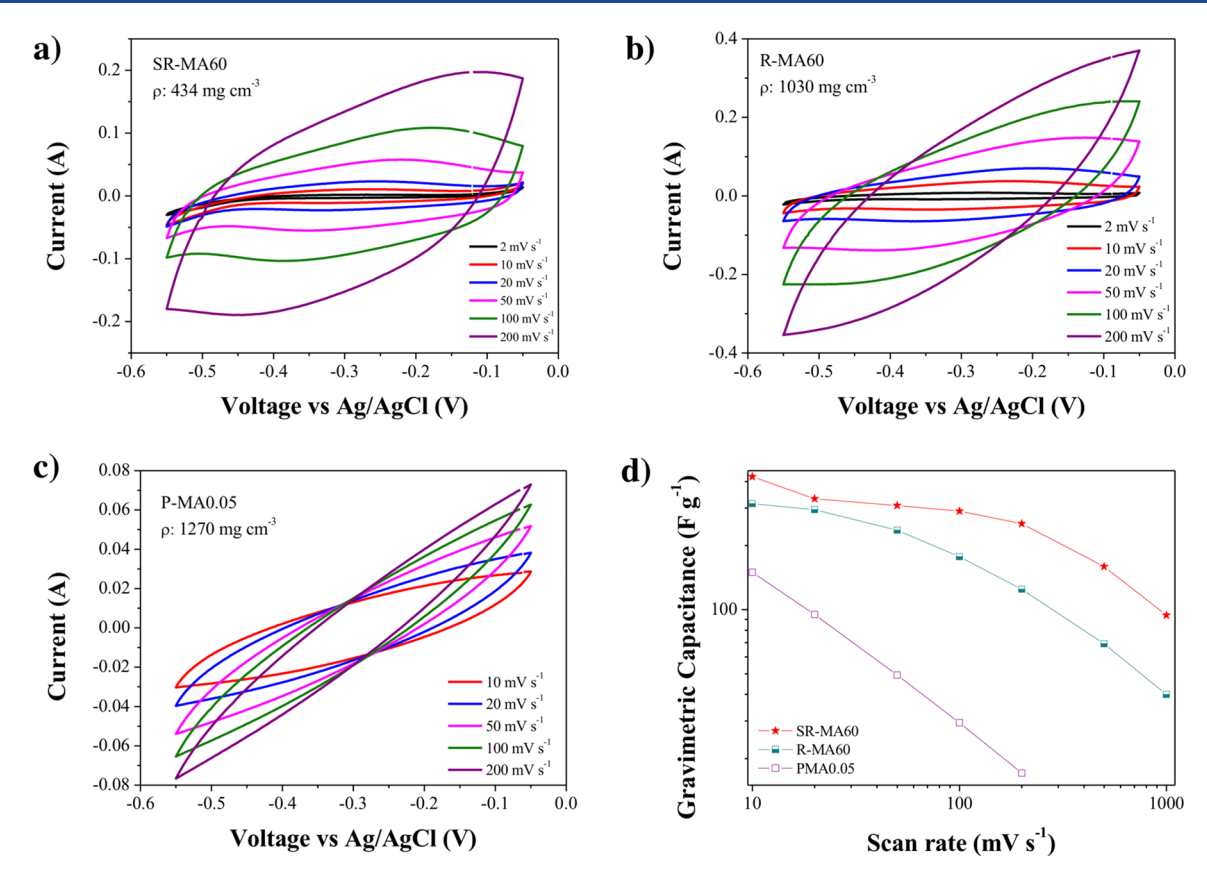


Figure 6. (a) CV profile of 60 μ m thick R-MA prepared from a slice of a MA (SR-MA60) at various scan rates (2 up to 200 mV s⁻¹). (b) CV profile of 60 μ m thick R-MA (R-MA60). (c) CV profile of 50 μ m P-MA (P-MA0.05). (d) Comparison of gravimetric capacitance as a function of samples with similar thickness prepared from different routes for different scan rates (from 2 to 200 mV s⁻¹). The densities (ρ) of each sample are included inside the corresponding graphs.

Our results show that the pressing of MAs stands as a promising approach to compensate for the gravimetric capacitance values with volumetric capacitance values and achieve higher power density, constituting a good starting point despite the poor rate capability of P-MAs (Figure S16a,b and S17a—c, and Table S2).

The rolling of P-MAs into thinner (167 to 50 μ m) and denser electrode layers (1030 to 375 mg cm⁻³) with optimized lamellae spacing (2 \pm 1 μ m for 85 μ m thin electrodes) via a calendering machine was proposed as a more effective and scalable method to improve the electrochemical performance (Figure S2). In this process, thickness is reduced homogeneously, while protecting the integrity of the lamellae structures and better preserving the accessible surface area (Table S4) and electrochemical behavior of the electrodes (Figure S13b, Figure 6, and Figure S18). As a consequence, rolling MA to denser electrodes improved the volumetric capacitance without sacrificing the gravimetric capacitance (Figure 5a,b, Figure 7a, and Figure S15). For example, 60 μ m thick electrodes with a density of 1030 mg cm⁻³ (R-MA60) reached a volumetric capacitance of 323 F cm⁻³ while maintaining a gravimetric capacitance of 315 F g⁻¹ at 10 mV s⁻¹. In addition, the electrochemical CV results for all R-MA samples (Figure 6a,b and Figure S17d-f) show redox/ intercalation peaks. In contrast, P-MAs possess a resistive nature and redox peaks are not observed (Figure 6c and Figure

To further improve the ion transport and charge storage within the electrode architectures, we rolled samples with a

similar thickness but with a lower density (less compacted samples) (Figure 6 and Figure S18). We prepared this type of sample (SR-MA) by rolling a slice of a standard aerogel (more details in the Methods section). In particular, less dense electrodes at 434 mg cm⁻³ (SR-MA60) presented improved capacitive performance with more pronounced redox/intercalation peaks when compared to denser electrodes (1030 mg cm⁻³) with the same thickness (R-MA60). The less compressed R-MA samples further demonstrated the best rate capability among the materials investigated in this work (Figures 6d and 7b).

The effects of electrode architectural features and processing route on the performance of different electrode forms investigated in this work (MA, P-MA and R-MA) are summarized and compared other electrodes in the literature in Figure 7 and Table S5.

Gravimetric vs Volumetric Capacitance. As shown in Figure 7a, while MAs can reach reasonable gravimetric capacitances at low densities, when their densities surpass an optimum (7–13 mg cm⁻³), both volumetric and gravimetric capacitances deteriorate with increasing density due to changes in their internal porous structures (Figure 2). Pressing of optimized MAs increases the density and consequently the volumetric capacitance of P-MAs. However, the process leads to losses in the lamellae architectural integrity due to the crumbling of lamellae what can reduce porous surface availability and the creation of wider gaps in between crumbled sites (Figures S15 and S18), deteriorating gravimetric capacitance and charge-transfer capability (Figure 7e). By

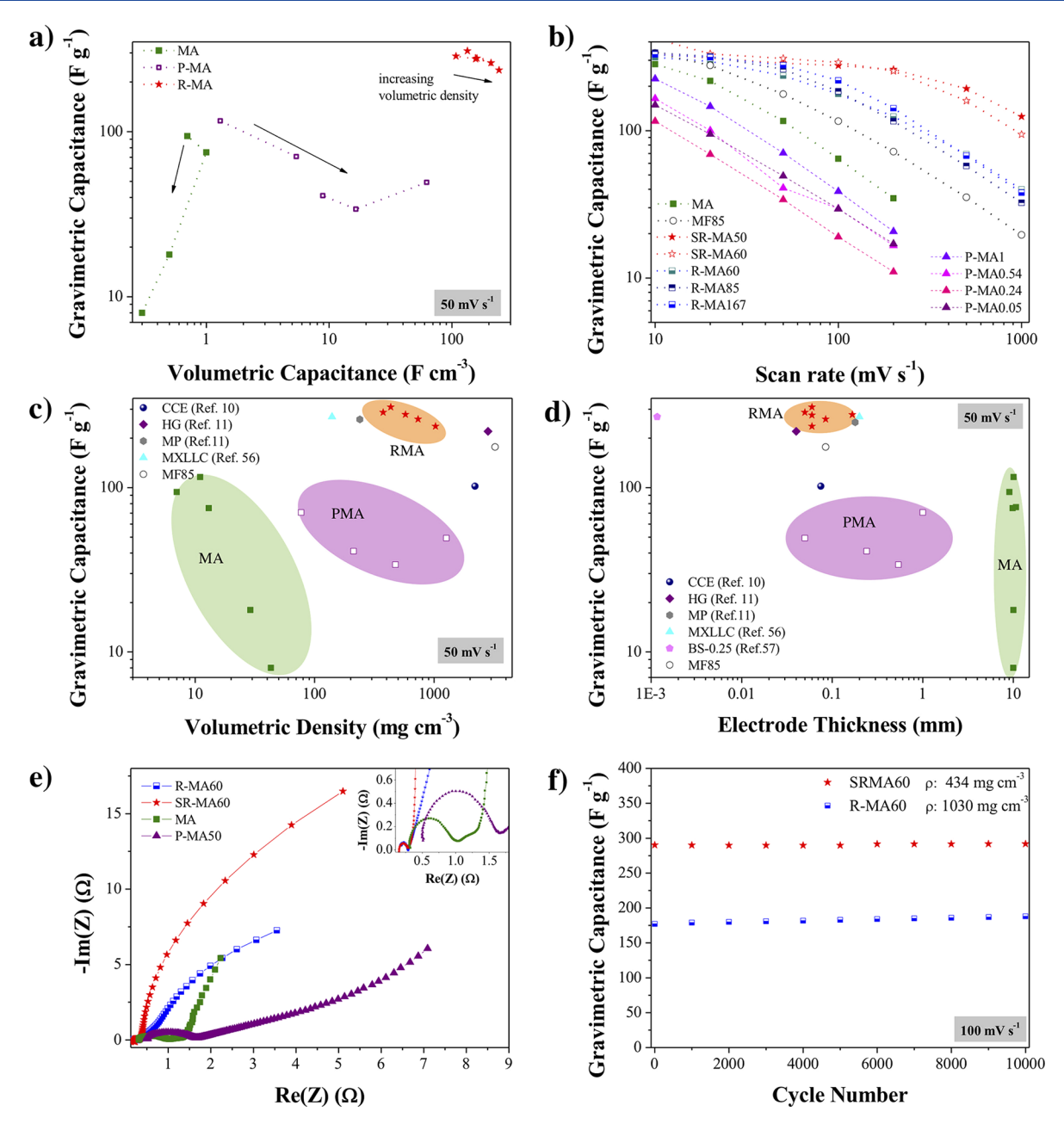


Figure 7. (a) Relation between gravimetric and volumetric capacitance for R-MAs, P-MAs, and MAs at 50 mV s⁻¹. Arrows indicate increase in density. (b) Rate performance based on gravimetric capacitance for R-MAs and P-MAs at various scan rates (20–1000 mV s⁻¹). (c, d) Gravimetric capacitance of MA, P-MA, and R-MA with respect to their volumetric densities and electrode thicknesses, respectively. The gravimetric capacitance obtained in this work are compared with other electrode structures of comparable density and thickness within current literature. Data taken from the literature are shown as follows: dark blue circles for 75 μm conductive clay electrode (CCE),¹⁰ purple diamonds for 40 μm hydrogel electrode (HG),¹¹ gray circles for 180 μm macroporous electrode (MP),¹¹ cyan triangles for 200 μm MXene lamellar liquid crystal (MXLLC),⁵⁶ and magenta pentagons for 1.17 μm bath-sonicated film (BS-0.25).⁵⁷ MF85 corresponds to 85 μm vacuum filtered electrodes produced in this work for comparison. (e) Impedance spectroscopy (EIS) of MA, P-MA, and R-MAs. P-MA and R-MAs have the same thickness with distinguished densities due to differences in preparation methods. (f) Cycling tests up to 10000 cycles for the two best performing R-MAs with the same thickness (SR-MA60 and R-MA60).

rolling the MA into thinner electrodes with preserved porous architectures (Figure S18), the volumetric capacitance can be improved over an order of magnitude while preserving the gravimetric capacitances at the highest levels. R-MAs continuous architectures also present the lowest charge-transfer resistance among the electrode types produced in this work (Figure 7e).

Rate Capability. While the optimized MA electrodes have considerably high gravimetric capacitance at low scan rates, the

performance drops by 88% upon increasing the scan rate from 10 to 200 mV s⁻¹ (Figure 7b). The highly porous nature of the aerogels (above 99% porosity, Figure S13a) and large pores (51 μ m average lamellae spacing, Figure 3a) can lead to a lengthy path, retarding ionic transport inside the architectures. R-MA electrodes achieve a considerable improvement in rate performance when compared to MAs and P-MAs, retaining up to 60% of their capacitance at 200 mV s⁻¹ (SR-MA60). The rate performance of 85 μ m thick R-MA (794 mg cm⁻³ density)

surpasses the performance of film electrodes with the same thickness (MF85 produced in this work for comparison) but 4 times its density (3250 mg cm⁻³) (Figure 7b-d and Table S2).

R-MAs Superior Performance. The superior capacitive performance of R-MAs (Figure 7c,d and Figure S13) can be first attributed to the optimized MA internal architecture that combines open porous, continuous lamellae ("prestructure" achieved via freeze-casting). In addition, the calendaring process allows them to be subsequently homogeneously compacted to denser structures with preserved electroactive internal walls of low charge-transfer resistance (impedance). This is achieved while retaining micrometer scale accessible pores (lamellae spacing of 1 \pm 0.6 μ m, Table S1 and Figure S18) for optimum ionic transport. As a consequence, R-MAs also possess excellent cycling performance, retaining 100.6% of their capacitive performance of 187.9 F g⁻¹ at 100 mV s⁻¹ without the disruption of the electrode structure after 10000 cycles (Figure 7f). Additionally, unlike current methods that utilize thermal processes to sacrifice the template and induce porosity, 11 unidirectional freeze-casting and calendering are both physically driven processes, and so the surface composition of the MXene flakes is not affected by their 3D assembly into electrodes. The versatility and scalability of the processing route, added to the electrodes' high performance and cycling ability, make the developed materials promising for practical applications.

CONCLUSIONS

In summary, we developed a simple and scalable route to fabricate high performance MXene electrodes by combining unidirectional freeze-casting with practical film processing methods. Freeze-casting allows the fabrication of ultralight MAs with optimized internal pore architectures for energy applications. In particular, open porous MAs with minimized bridging within lamellae can deliver gravimetric capacitance values of up to 380 F g⁻¹ at 2 mV s⁻¹. While pressing of MAs with a simple setup increases their volumetric capacitance (from 3 to 56 F cm⁻³ at 10 mV s⁻¹), the calendering into denser (up to 1 g cm⁻³) electrode films (R-MAs) leads to a considerable improvement in volumetric capacitances while maintaining the high gravimetric capacitances (322.8 F cm⁻³ and 315 F g⁻¹ at 10 mV s⁻¹). The R-MAs architectures with appropriate thickness and density reach rate capabilities among the highest for MXene electrodes with comparable thicknesses or density (60 μ m thick, 434 mg cm⁻³ R-MAs reached 308.8 F g⁻¹ capacitance at 50 mV s⁻¹). R-MAs open up practical opportunities in the development of energy storage devices with high power and energy densities and the fabrication route developed here can serve as a guide to tune the electrodes' internal porous architectures to maximize performance. In particular, optimized performance can be achieved by a combination of open porous, continuous lamellar architectures with an appropriate lamella spacing for ionic transport. By further optimizations in 2D MXene chemistry and morphology, fabrication, and testing conditions, even higher volumetric capacitance and rate capabilities could be achieved. We anticipate that these findings can be extended to the development of MXene tuned porous architectures for a wide range of applications from energy, catalysis, and environmental cleaning to electromagnetic interference (EMI) shielding among others.

METHODS

Synthesis of 2D Ti₃C₂T_x. Ti₃AlC₂ powder is the precursor for Ti₃C₂T_x synthesis and was produced in Drexel University according to the method mentioned in previous studies. 10 The etching solution is prepared by dissolving 7.5 mol equiv of lithium fluoride (LiF, Alfa Aesar, 98+%) in 9 M hydrochloric acid (HCl, Alfa Aesar, 36.5-38.0% and dilution with deionized water) inside a HDPE reaction vessel. The solution was heated to 40 °C inside an oil bath. Three grams of Ti₃AlC₂ powder was slowly added to the solution under vigorous stirring. The reaction was kept at 40 °C for 24 h. After 24 h, the reaction mixture was diluted with DI water and transferred into centrifuge bottles. The reaction mixture was centrifuged at 3500 rpm (1876g, Sorvall Legend XTR centrifuge) and washed with DI water several times until pH reached 6. The supernatant which was still black in color (showing the presence of suspended $Ti_3C_2T_x$ flakes) was separated from the sediment. N2 was purged into the solution, and the cap of the bottle was closed and sealed.

Preparation of Stock Solutions for Freeze-Casting. The N₂purged solution was sonicated for 1 h in bath sonication at 20 °C with continuous cooling to avoid heat generation which might result in oxidation of the Ti₃C₂T_r flakes. After sonication, the mixtures were centrifuged at 1000 rpm for 1 h. The supernatant was transferred into a separate bottle, N2-purged, sealed with Parafilm, labeled as Ti3C2Tx stock solution, and stored in a fridge at 2 °C. The concentration of the solution was determined via freezing and freeze-drying small volumes of the solution and weighing the solid amount per unit volume. The concentration prior to freeze-casting was adjusted via dilution or concentrating the stock solution.

Preparation of Filtered Ti₃C₂T_x "Film" Electrodes (MFs). A desired volume from ${\rm Ti}_3{\rm C}_2{\rm T}_x$ stock solution was diluted to obtain a suspension with 0.2 g mL $^{-1}$ concentration. The suspension was filtered through a mixed cellulose ester (MCE) membrane filter with 0.45 µm pore size (Shanghai Xingya purifying material factory, Shanghai, China) and dried inside a vacuum oven at room temperature. 10,58 The filtered film was detached from the membrane after the vacuum-drying process. The films were cut into desired electrode area and weighed prior to electrochemical testing. The density of the filtered $Ti_3C_2T_x$ films was 3.25 g cm⁻³.

Preparation of $Ti_3C_2T_x$ Aerogels via Freeze-Casting. The $Ti_3C_2T_x$ suspensions with specific concentrations (5–50 mg mL⁻¹) are poured into Teflon molds with a copper base and are subsequently fitted on the top of the freeze caster copper finger (Figure S1). During direction freezing suspensions are frozen from 20 down to −60 °C at controlled freezing rates of 2.5 or 5 °C min⁻¹. The samples were kept at -60 °C for 15 min. The frozen samples were demolded and directly placed inside a freeze-dryer (Freezone Labcanco benchtop 6 L freeze-dryer, USA) during 2 days for complete freeze-drying. The dimension and weight of the samples were determined by using a caliper with an accuracy of 0.01 mm (DURATOOL) and a weighing balance (OHAUS AX324) with an accuracy of 0.001 g. The volumetric densities of MAs and other electrode structures (P-MA and R-MA) were calculated with the formula $\rho = \frac{\nu}{m}$, where ν is the volume (obtained by the multiplication of dimensional lengths) and *m* is the mass of the sample. The densities of the MAs ranged between 7 and 43 mg cm⁻³ (Table S1). The skeletal density of Ti₃C₂T_x was measured by a He pycnometer and found to be 3.15 g cm⁻³. The porosity measurements were calculated via the formula $\varepsilon = 1 - \rho/\rho_0$, where ρ is the density of samples and ρ is the skeletal density of $Ti_3C_2T_x$

Preparation of Pressed (P-MAs) and Rolled Ti₃C₂T_x MXene Aerogels (R-MAs). Two PMMA plates were utilized to compress MA from the side walls to a certain thickness (controlled with a digital micrometer (Mitutoyo) with a resolution of 0.001 mm and an accuracy of ±0.001 mm) and stabilized with screws on both sides (Figure S9c,d). This alignment was chosen due to their strongly aligned unidirectional lamellae structure from top to bottom and pressing perpendicular to the freezing direction results in less damage to the aerogel structure. The dimension and weight of the samples were determined by using the digital micrometer and a weighing balance (OHAUS AX324) with an accuracy of 0.001 g. The densities of P-MAs ranged between 77 and 1270 mg cm⁻³.

The spacing between two rolls within the calendering machine was controlled and adjusted with a leaf tapered feeler gauge (0.03–0.5 mm) according to the desired thickness of the final electrode layer (Figure S2). An MA or a vertical slice of an MA was pressed prior to calendering. After achieving a thickness that would allow the MA to roll through the calendering machine homogeneously on the contact surface, the benchtop calendering machine operated on a forward direction to roll P-MAs into a slice-rolled MA (SR-MA) or an MA (R-MA). The thickness of R-MA or SR-MA was measured with a digital micrometer (Mitutoyo) with a resolution of 0.001 mm and an accuracy of ± 0.001 mm. If the desired thickness was not obtained, the rolling process was repeated to reach the desired value. The densities of R-MAs ranged between 375 and 1030 mg cm⁻³.

Electrochemical Measurements. All electrochemical measurements were performed in three-electrode cells with 3 M H₂SO₄ (Acros Organics, 96%) aqueous electrolyte. Three electrode cell testing of MAs, MFs, P-MAs, and R-MAs was conducted in a beaker setup with respect to a Ag/AgCl standard reference electrode. The observed structural stability of the electrodes allowed the electrochemical tests within this beaker type setup without using additional support. For better comparison with literature data, MFs were also tested in a three-electrode Swagelok cell (Figure S19). The working electrodes were prepared by connecting stainless-steel mesh (Dextmet 5SS (316L)-7) current collectors inside the MAs. For P-MAs, stainless steel mesh was placed in the middle of an MA prior to compression, and later, two PMMA plates were utilized to compress MA from side walls to a certain thickness and stabilized with screws on both sides (Figure S9c,d). The R-MAs were placed on a stainlesssteel mesh and stabilized with another stainless-steel mesh on top

Activated carbon cloth (Kynol Europa GmbH ACC-507-20) was used as the counter electrode, and stainless steel (Dextmet SSS (316L)-7) was used as the current collector. All CV (cyclic voltammetry) and GCD (galvanostatic charge/discharge curves) measurements were conducted on an IviumStat electrochemical workstation. Electrochemical impedance spectroscopy (EIS) data were collected in the 100 mHz–100 kHz range by using a potential amplitude of 10 mV. Cycling tests were conducted at 100 mV s⁻¹ up to 10000 cycles.

Capacitance Calculations. The specific capacitance of electrodes was calculated both from CV and GCD (galvanostatic charge—discharge curves). The calculations were based on $C_t = \frac{\int I \Delta t}{\Delta V}$ and $C_s = \frac{C_t}{m_t}$ where C_t is total capacitance of the device. The specific capacitance, C_s , is calculated by dividing C_t with m_t , which is the mass of the working electrode. I is the current, and its integration over discharging time is equal to $Q_{\rm discharging}$. $Q_{\rm discharging}$ is the charge delivered during the discharge half-cycle. The total capacitance is equal to $C_t = \frac{Q_{\rm discharging}}{\Delta V}$, where ΔV is the operating voltage range of the specific supercapacitor electrode.

Trasatti Measurements. The diffusion-limited and surface capacitive contributions in total capacitance were calculated by the Trasatti method, $i(v) = k_1 v + k_2 v^{1/2}$. The surface capacitive contributions of the electric double-layer (EDL) and surface redox reactions, was obtained by using the gravimetric capacitance values of MAs, P-MAs R-MAs, and SR-MAs and plotting them with respect to the inverse square root of scan rate $(v^{-1/2})$. The total achievable capacitance of MAs and P-MAs was obtained by plotting the inverse gravimetric capacitance values versus square root of scan rate $(v^{1/2})$. The diffusion-limited capacitance values were obtained by subtraction of the surface related capacitance (the combination of EDL and surface redox reactions) from the total capacitance (assuming on $Q_t = Q_t + Q_o$ where Q_t is total capacitance and Q_i and Q_o are inner and outer capacitance, respectively).

Characterization of Structure and Properties of 2D $Ti_3C_2T_x$ and $Ti_3C_2T_x$ Aerogels. XRD measurements were taken with a

PANalytical XPERT-PRO using Cu Klpha radiation at a step size of 0.033 between $2\theta = 5^{\circ}-60^{\circ}$. Scanning electron microscope (SEM) secondary electron images were taken with a Zeiss EVO 60, a Philips XL30 FEGSEM, and a Tescan SC MIRA 3 FEGSEM. Atomic force microscopy (AFM) images were taken via a Dimension 3100 atomic force microscope. Average values for the flake size, pore size, and wall opening were obtained from over a hundred measurements of the features using ImageJ software. Electron transparent samples were prepared for scanning transmission electron microscope (STEM) imaging by dusting crushed aerogels onto holey carbon 300 mesh Cu TEM support films. STEM annular dark field (ADF) images were taken with a FEI Titan G2 ChemiSTEM operating at 200 kV with a 180 pA beam current, a probe convergence angle of 21 mrad, and an inner ADF acceptance angle of 54 mrad. Images were processed with Gatan's Digital micrograph software. Synchrotron X-ray microtomography (Micro CT) was performed at the European Synchrotron Radiation Facility by using the ID15A beamline to image samples compressed by 50% and 70% and in the uncompressed state (having sample heights of 5, 3, and 10 mm, respectively). Imaging was performed at 40 keV energy and 100 ms exposure time, taking 1500 projections around 180° of sample rotation. A 2560 × 2160 $(h \times v)$ 6.5 μ m pixel pco.edge CCD camera was used to collect the X-ray projections, coupled to a 2× microscope objective, giving an effective pixel size of 3.2 μ m and a field-of-view of ~4.4 mm.

The sample-to-detector distance was 100 mm to allow some in-line phase contrast to enhance visibility of the aerogel sheets. Reconstruction was performed using a filtered back projection algorithm, and visualization was performed by using an Avizo (Thermo Fisher Scientific). The specific surface area and pore size were determined by using a Quadrasorb Evo, using the Brunauer–Emmett–Teller (BET) method (specific surface area) and Barrett–Joyner– Halenda (BJH) method for pore size. To ensure the reliability of measurements, >100 mg of samples was used. All samples were degassed for 36 h under 0.01 mbar and at 333 K before the nitrogen adsorption. The nitrogen adsorption isotherms were performed at relative pressures (P/P_0) between 0.004 and 1 at a bath temperature of 77 K with 40 points for adsorption and 39 points for desorption. Zeta-potential values for MXene suspension were taken with a Zetasizer Nano ZS by Malvern Instruments.

ASSOCIATED CONTENT

S Supporting Information

The Supporting Information is available free of charge at https://pubs.acs.org/doi/10.1021/acsaem.9b01654.

Images of lab-built freeze-caster and electrochemical testing setup, diagram of pressing and rolling MAs into P-MAs and R-MAs, the logical path for electrode fabrication, analysis of $\mathrm{Ti_3C_2T_x}$ flakes with AFM, SEM, XRD, and STEM, CVs of individual electrodes, Trasatti measurements, comparative graphs for gravimetric and volumetric capacitance of the electrodes with respect to their volumetric densities, Micro-CT and binary images of P-MAs, SEM of P-MAs, R-MAs, and SR-MAs, CV of MF obtained with Swagelok cell test, table of freeze-casting parameters, pore sizes, and porosity parameters, tables of capacitance values for the electrodes, table of SSA values obtained from BET, table of the electrochemical performances' comparison with current literature (PDF)

AUTHOR INFORMATION

Corresponding Author

*E-mail: Suelen.barg@manchester.ac.uk.

ORCID (

Shelley D. Rawson: 0000-0002-9407-4072 Sarah J. Haigh: 0000-0001-5509-6706

Michel W. Barsoum: 0000-0001-7800-3517 Ian A. Kinloch: 0000-0003-3314-6869 Suelen Barg: 0000-0002-0723-7081

Author Contributions

S.B., V.B., and I.A.K. devised the original concept, designed the experiments, discussed the interpretation of results, and revised the paper. V.B. performed all the experiments. V.B. wrote the draft of the manuscript. M.G. and M.W.B. synthesized and provided MAX powder. M.G. provided guidance on MXene synthesis and helped in the materials characterization. S.D.R., S.A.M., P.Y., and P.J.W. contributed to perform Micro-CT on aerogel samples as well as the reconstruction and visualization of Micro CT images. J.J.B. helped on SEM, EIS, BET, and cycling tests. M.L., S.F., and S.J.H. contributed by taking and analyzing STEM images. All authors participated in manuscript revision.

Notes

The authors declare no competing financial interest.

ACKNOWLEDGMENTS

V.B. thanks the Newton-Katip Celebi Fund provided by The Scientific and Technological Research Council of Turkey (TUBITAK) and British Council. S.B., V.B., S.D.R., P.Y., S.A.M., and P.J.W. thank the European Research Council for the funding given for Micro-CT studies, which was provided under the European Commission's Horizon 2020 (FP8/2014-2020) ERC grant agreement number 695638 (CORREL-CT). The authors also acknowledge the European Synchrotron Radiation Facility (ESRF) for provision of synchrotron radiation facilities at beamline ID15A, and they are grateful for the support of Thomas Buslaps for assistance in setting up the instrument. S.J.H. and S.F. thank the U.K. Engineering and Physical Sciences Research Council (EPSRC) (EP/P009050/ 1) and the European Research Council (ERC) under the European Union's Horizon 2020 research and innovation program (Grant Agreement ERC-2016-STG-EvoluTEM-715502). M.G. and M.W.B. were supported by the NSF (DMR-1740795).

REFERENCES

- (1) Simon, P.; Gogotsi, Y. Materials for Electrochemical Capacitors. Nat. Mater. 2008, 7 (11), 845-854.
- (2) Liu, C.; Li, F.; Ma, L.-P.; Cheng, H.-M. Advanced Materials for Energy Storage. Adv. Mater. 2010, 22 (8), E28-E62.
- (3) Mendoza-Snchez, B.; Gogotsi, Y. Synthesis of Two-Dimensional Materials for Capacitive Energy Storage. Adv. Mater. 2016, 28, 6104-
- (4) Zhang, L. L.; Gu, Y.; Zhao, X. S. Advanced Porous Carbon Electrodes for Electrochemical Capacitors. J. Mater. Chem. A 2013, 1 (33), 9395.
- (5) Miller, J. R.; Simon, P. Electrochemical Capacitors for Energy Management. Science (Washington, DC, U. S.) 2008, 321 (5889), 651-652.
- (6) Goodenough, J. B. Energy Storage Materials: A Perspective 2015,
- (7) Zhang, X.; Zhang, Z.; Zhou, Z. MXene-Based Materials for Electrochemical Energy Storage. J. Energy Chem. 2018, 27, 73.
- (8) Anasori, B.; Lukatskaya, M. R.; Gogotsi, Y. 2D Metal Carbides and Nitrides (MXenes) for Energy Storage. Nat. Rev. Mater. 2017, 2, 16098
- (9) Hope, M. A.; Forse, A. C.; Griffith, K. J.; Lukatskaya, M. R.; Ghidiu, M.; Gogotsi, Y.; Grey, C. P. NMR Reveals the Surface Functionalisation of Ti 3 C 2 MXene. Phys. Chem. Chem. Phys. 2016, 18 (7), 5099-5102.

- (10) Ghidiu, M.; Lukatskaya, M. R.; Zhao, M.; Gogotsi, Y.; Barsoum, M. W. Conductive Two-Dimensional Titanium Carbide 'Clay' with High Volumetric Capacitance. Nature 2014, 516 (7529), 78-81.
- (11) Lukatskaya, M. R.; Kota, S.; Lin, Z.; Zhao, M.-Q.; Shpigel, N.; Levi, M. D.; Halim, J.; Taberna, P.-L.; Barsoum, M. W.; Simon, P.; Gogotsi, Y. Ultra-High-Rate Pseudocapacitive Energy Storage in Two-Dimensional Transition Metal Carbides. Nat. Energy 2017, 2 (8),
- (12) Naguib, M.; Mashtalir, O.; Carle, J.; Presser, V.; Lu, J.; Hultman, L.; Gogotsi, Y.; Barsoum, M. W. Two-Dimensional Transition Metal Carbides. ACS Nano 2012, 6 (2), 1322-1331.
- (13) Naguib, M.; Kurtoglu, M.; Presser, V.; Lu, J.; Niu, J.; Heon, M.; Hultman, L.; Gogotsi, Y.; Barsoum, M. W. Two-Dimensional Nanocrystals Produced by Exfoliation of Ti 3AlC 2. Adv. Mater. **2011**, 23 (37), 4248–4253.
- (14) Chang, F.; Li, C.; Yang, J.; Tang, H.; Xue, M. Synthesis of a New Graphene-like Transition Metal Carbide by de-Intercalating Ti3AlC2. Mater. Lett. 2013, 109, 295-298.
- (15) Alhabeb, M.; Maleski, K.; Anasori, B.; Lelyukh, P.; Clark, L.; Sin, S.; Gogotsi, Y. Guidelines for Synthesis and Processing of Two-Dimensional Titanium Carbide (Ti 3 C 2 T x MXene). Chem. Mater. 2017, 29 (18), 7633-7644.
- (16) Barsoum, M. W. The Mn+1AXn Phases: A New Class of Solids. Prog. Solid State Chem. 2000, 28, 201-281.
- (17) Lukatskaya, M. R.; Mashtalir, O.; Ren, C. E.; Dall'Agnese, Y.; Rozier, P.; Taberna, P. L.; Naguib, M.; Simon, P.; Barsoum, M. W.; Gogotsi, Y. Cation Intercalation and High Volumetric Capacitance of Two-Dimensional Titanium Carbide. Science (Washington, DC, U. S.) **2013**, 341 (6153), 1502–1505.
- (18) Mashtalir, O.; Naguib, M.; Mochalin, V. N.; Dall'Agnese, Y.; Heon, M.; Barsoum, M. W.; Gogotsi, Y. Intercalation and Delamination of Layered Carbides and Carbonitrides. Nat. Commun. 2013, 4, 1716.
- (19) Zhao, M.-Q.; Ren, C. E.; Ling, Z.; Lukatskaya, M. R.; Zhang, C.; Van Aken, K. L.; Barsoum, M. W.; Gogotsi, Y. Flexible MXene/ Carbon Nanotube Composite Paper with High Volumetric Capacitance. Adv. Mater. 2015, 27 (2), 339-345.
- (20) Yan, P.; Zhang, R.; Jia, J.; Wu, C.; Zhou, A.; Xu, J.; Zhang, X. Enhanced Supercapacitive Performance of Delaminated Two-Dimensional Titanium Carbide/Carbon Nanotube Composites in Alkaline Electrolyte. J. Power Sources 2015, 284, 38-43.
- (21) Li, L.; Zhang, M.; Zhang, X.; Zhang, Z. New Ti3C2 Aerogel as Promising Negative Electrode Materials for Asymmetric Supercapacitors. J. Power Sources 2017, 364, 234-241.
- (22) Xie, X.; Zhao, M.-Q.; Anasori, B.; Maleski, K.; Ren, C. E.; Li, J.; Byles, B. W.; Pomerantseva, E.; Wang, G.; Gogotsi, Y. Porous Heterostructured MXene/Carbon Nanotube Composite Paper with High Volumetric Capacity for Sodium-Based Energy Storage Devices. Nano Energy 2016, 26, 513-523.
- (23) Zhao, C.; Wang, Q.; Zhang, H.; Passerini, S.; Qian, X. Two-Dimensional Titanium Carbide/RGO Composite for High-Performance Supercapacitors. ACS Appl. Mater. Interfaces 2016, 8 (24), 15661-15667.
- (24) Luo, J.; Zhang, W.; Yuan, H.; Jin, C.; Zhang, L.; Huang, H.; Liang, C.; Xia, Y.; Zhang, J.; Gan, Y.; Gan, Y.; Tao, X. Pillared Structure Design of MXene with Ultralarge Interlayer Spacing for High-Performance Lithium-Ion Capacitors. ACS Nano 2017, 11 (3), 2459-2469.
- (25) Liu, J.; Zhang, H.-B.; Sun, R.; Liu, Y.; Liu, Z.; Zhou, A.; Yu, Z.-Z. Hydrophobic, Flexible, and Lightweight MXene Foams for High-Performance Electromagnetic-Interference Shielding. Adv. Mater. 2017, 29, 1702367.
- (26) Zhao, M.-Q.; Xie, X.; Ren, C. E.; Makaryan, T.; Anasori, B.; Wang, G.; Gogotsi, Y. Hollow MXene Spheres and 3D Macroporous MXene Frameworks for Na-Ion Storage. Adv. Mater. 2017, 29 (37), 1702410.
- (27) Shah, S.; Habib, T.; Gao, H.; Gao, P.; Sun, W.; Green, M.; Radovic, M. Template-Free 3D Titanium Carbide (Ti3C2Tx) MXene

- Particles Crumpled by Capillary Forces. Chem. Commun. 2017, 53, 400-403.
- (28) Natu, V.; Clites, M.; Pomerantseva, E.; Barsoum, M. W. Mesoporous MXene Powders Synthesized by Acid Induced Crumpling and Their Use as Na-Ion Battery Anodes. *Mater. Res. Lett.* **2018**, *6* (4), 230–235.
- (29) Yue, Y.; Liu, N.; Ma, Y.; Wang, S.; Liu, W.; Luo, C.; Zhang, H.; Cheng, F.; Rao, J.; Hu, X.; Su, J.; Gao, Y. Highly Self-Healable 3D Microsupercapacitor with MXene—Graphene Composite Aerogel. ACS Nano 2018, 12 (5), 4224–4232.
- (30) Ma, Y.; Yue, Y.; Zhang, H.; Cheng, F.; Zhao, W.; Rao, J.; Luo, S.; Wang, J.; Jiang, X.; Liu, Z.; Liu, N.; Gao, Y. 3D Synergistical MXene/Reduced Graphene Oxide Aerogel for a Piezoresistive Sensor. *ACS Nano* **2018**, *12* (4), 3209–3216.
- (31) Bao, W.; Tang, X.; Guo, X.; Choi, S.; Wang, C.; Gogotsi, Y.; Wang, G. Porous Cryo-Dried MXene for Efficient Capacitive Deionization. *Joule* **2018**, 2 (4), 778–787.
- (32) Han, M.; Yin, X.; Hantanasirisakul, K.; Li, X.; Iqbal, A.; Hatter, C. B.; Anasori, B.; Koo, C. M.; Torita, T.; Soda, Y.; Zhang, L.; Cheng, L.; Gogotsi, Y. Anisotropic MXene Aerogels with a Mechanically Tunable Ratio of Electromagnetic Wave Reflection to Absorption. *Adv. Opt. Mater.* **2019**, *7*, 1900267.
- (33) Deville, S. Ice-Templating, Freeze Casting: Beyond Materials Processing. J. Mater. Res. 2013, 28 (17), 2202–2219.
- (34) Deville, S.; Saiz, E.; Tomsia, A. P. Ice-Templated Porous Alumina Structures. *Acta Mater.* **2007**, *55* (6), 1965–1974.
- (35) D'Elia, E.; Barg, S.; Ni, N.; Rocha, V. G.; Saiz, E. Self-Healing Graphene-Based Composites with Sensing Capabilities. *Adv. Mater.* **2015**, 27 (32), 4788–4794.
- (36) Wu, X.; Tang, L.; Zheng, S.; Huang, Y.; Yang, J.; Liu, Z.; Yang, W.; Yang, M. Hierarchical Unidirectional Graphene Aerogel/Polyaniline Composite for High Performance Supercapacitors. *J. Power Sources* **2018**, 397, 189–195.
- (37) Wang, Z.; Shen, X.; Han, N. M.; Liu, X.; Wu, Y.; Ye, W.; Kim, J. K. Ultralow Electrical Percolation in Graphene Aerogel/Epoxy Composites. *Chem. Mater.* **2016**, 28 (18), 6731–6741.
- (38) Han, N. M.; Wang, Z.; Shen, X.; Wu, Y.; Liu, X.; Zheng, Q.; Kim, T. H.; Yang, J.; Kim, J. K. Graphene Size-Dependent Multifunctional Properties of Unidirectional Graphene Aerogel/Epoxy Nanocomposites. ACS Appl. Mater. Interfaces 2018, 10 (7), 6580–6592.
- (39) Zhang, H.; Cooper, A. I. Aligned Porous Structures by Directional Freezing. Adv. Mater. 2007, 19 (11), 1529–1533.
- (40) Akuzum, B.; Maleski, K.; Anasori, B.; Lelyukh, P.; Alvarez, N. J.; Kumbur, E. C.; Gogotsi, Y. Rheological Characteristics of 2D Titanium Carbide (MXene) Dispersions: A Guide for Processing MXenes. ACS Nano 2018, 12 (3), 2685–2694.
- (41) Zhu, C.; Han, T. Y.-J.; Duoss, E. B.; Golobic, A. M.; Kuntz, J. D.; Spadaccini, C. M.; Worsley, M. A. Highly Compressible 3D Periodic Graphene Aerogel Microlattices. *Nat. Commun.* **2015**, *6*, 6962.
- (42) Urbankowski, P.; Anasori, B.; Makaryan, T.; Er, D.; Kota, S.; Walsh, P. L.; Zhao, M.; Shenoy, V. B.; Barsoum, M. W.; Gogotsi, Y. Synthesis of Two-Dimensional Titanium Nitride Ti 4 N 3 (MXene). *Nanoscale* **2016**, *8* (22), 11385–11391.
- (43) Sharma, R.; Chadha, N.; Saini, P. Determination of Defect Density, Crystallite Size and Number of Graphene Layers in Graphene Analogues Using X-Ray Diffraction and Raman Spectroscopy. *Indian J. Pure Appl. Phys.* **2017**, 55 (9), 625–629.
- (44) Deville, S.; Saiz, E.; Nalla, R. K.; Tomsia, A. P. Freezing as a Path to Build Complex Composites. *Science (Washington, DC, U. S.)* **2006**, 311 (5760), 515–518.
- (45) Zhang, H.; Cooper, A. I. Aligned Porous Structures by Directional Freezing. *Adv. Mater.* **2007**, *19* (11), 1529–1533.
- (46) Yang, M.; Zhao, N.; Cui, Y.; Gao, W.; Zhao, Q.; Gao, C.; Bai, H.; Xie, T. Biomimetic Architectured Graphene Aerogel with Exceptional Strength and Resilience. *ACS Nano* **2017**, *11* (7), 6817–6824.

- (47) Zou, J.; Zhang, Y.; Li, R. Effect of Suspension State on the Pore Structure of Freeze-Cast Ceramics. *Int. J. Appl. Ceram. Technol.* **2011**, 8 (2), 482–489.
- (48) Deville, S. Freezing as a Path to Build Complex Composites. Science (Washington, DC, U. S.) 2006, 311 (5760), 515-518.
- (49) Xu, T.; Wang, C. A. Control of Pore Size and Wall Thickness of 3–1 Type Porous PZT Ceramics during Freeze-Casting Process. *Mater. Des.* **2016**, *91*, 242.
- (50) Lee, J. S. M.; Briggs, M. E.; Hu, C. C.; Cooper, A. I. Controlling Electric Double-Layer Capacitance and Pseudocapacitance in Heteroatom-Doped Carbons Derived from Hypercrosslinked Microporous Polymers. *Nano Energy* **2018**, *46*, 277.
- (51) Li, L.; Zhang, N.; Zhang, M.; Zhang, X.; Zhang, Z. Flexible Ti 3 C 2 T x /PEDOT:PSS Films with Outstanding Volumetric Capacitance for Asymmetric Supercapacitors. *Dalt. Trans.* **2019**, 48 (5), 1747–1756.
- (52) Ni, N.; Barg, S.; Garcia-Tunon, E.; Macul Perez, F.; Miranda, M.; Lu, C.; Mattevi, C.; Saiz, E. Understanding Mechanical Response of Elastomeric Graphene Networks. *Sci. Rep.* **2015**, *5* (1), 13712.
- (53) Hong, J.-Y.; Bak, B. M.; Wie, J. J.; Kong, J.; Park, H. S. Reversibly Compressible, Highly Elastic, and Durable Graphene Aerogels for Energy Storage Devices under Limiting Conditions. *Adv. Funct. Mater.* **2015**, *25* (7), 1053–1062.
- (54) Lin, Y.; Liu, F.; Casano, G.; Bhavsar, R.; Kinloch, I. A.; Derby, B. Pristine Graphene Aerogels by Room-Temperature Freeze Gelation. *Adv. Mater.* **2016**, 28 (36), 7993–8000.
- (55) Wang, J.; Polleux, J.; Lim, J.; Dunn, B. Pseudocapacitive Contributions to Electrochemical Energy Storage in TiO 2 (Anatase) Nanoparticles. *J. Phys. Chem. C* **2007**, *111* (40), 14925–14931.
- (56) Xia, Y.; Mathis, T. S.; Zhao, M. Q.; Anasori, B.; Dang, A.; Zhou, Z.; Cho, H.; Gogotsi, Y.; Yang, S. Thickness-Independent Capacitance of Vertically Aligned Liquid-Crystalline MXenes. *Nature* **2018**, 557 (7705), 409–412.
- (57) Maleski, K.; Ren, C. E.; Zhao, M. Q.; Anasori, B.; Gogotsi, Y. Size-Dependent Physical and Electrochemical Properties of Two-Dimensional MXene Flakes. ACS Appl. Mater. Interfaces 2018, 10 (29), 24491–24498.
- (58) Ling, Z.; Ren, C. E.; Zhao, M.-Q.; Yang, J.; Giammarco, J. M.; Qiu, J.; Barsoum, M. W.; Gogotsi, Y. Flexible and Conductive MXene Films and Nanocomposites with High Capacitance. *Proc. Natl. Acad. Sci. U. S. A.* **2014**, *111* (47), 16676–16681.
- (59) Liu, Y.; Qian, W.; Zhang, Q.; Cao, A.; Li, Z.; Zhou, W.; Ma, Y.; Wei, F. Hierarchical Agglomerates of Carbon Nanotubes as High-Pressure Cushions. *Nano Lett.* **2008**, *8*, 1323.
- (60) Sankar, K. V.; Selvan, R. K. The Ternary MnFe2O4/Graphene/Polyaniline Hybrid Composite as Negative Electrode for Supercapacitors. *J. Power Sources* **2015**, *275*, 399–407.
- (61) Liu, C.; Gillette, E. I.; Chen, X.; Pearse, A. J.; Kozen, A. C.; Schroeder, M. A.; Gregorczyk, K. E.; Lee, S. B.; Rubloff, G. W. An Allin-One Nanopore Battery Array. *Nat. Nanotechnol.* **2014**, *9* (12), 1031–1039.